ARTICLE   OPEN

Qubit-controlled directional edge states in waveguide QED

Prasanna Pakkiam [ID][1 ✉], N. Pradeep Kumar[1], Mikhail Pletyukhov [ID][2] and Arkady Fedorov[1]

We propose an in-situ tunable chiral quantum system, composed of a quantum emitter coupled to a waveguide based on the Rice-Mele model (where we alternate both the on-site potentials and tunnel couplings between sites in the waveguide array). Specifically, we show that the chirality of photonic bound state, that emerges in the bandgap of the waveguide, depends only on the energy of the qubit; a parameter that is easy to tune in many artificial atoms. In contrast to previous proposals that have either shown imperfect chirality or fixed directionality, our waveguide quantum electrodynamics scheme achieves both perfect chirality and the capability to switch the directionality on demand with just one tunable element in the device. We also show that our model is easy to implement in both state-of-the-art superconducting circuit and quantum dot architectures. The results show technological promise in creating long-range couplers between qubits while maintaining, in principle, zero crosstalk.

INTRODUCTION

Engineering interactions between distant quantum emitters mediated by photons travelling in a 1D waveguide is crucial for building large scale quantum networks[1]. In particular, realising chiral light-matter interaction that results in unidirectional emission and scattering of photons can enable routing of quantum information between different nodes[2] and can also aid in on-chip integration of non-reciprocal devices such as single-photon diodes, transistors, circulators and amplifiers[3–6]. Furthermore, such chiral interactions has far reaching applications in probing complex many body quantum states[7–9]. Remarkable experimental progress has also been made in realizing such interactions in a variety of waveguide quantum electrodynamics (wQED) platforms. More specifically, in nanophotonic waveguides such as nanofibers and photonic crystals, spin-momentum locking between quantum emitters and the guided modes has led to the observation of asymmetric spontaneous emission of photons[10,11].

Distinctly different chiral quantum phenomenon has also been demonstrated in superconducting qubits coupled to a 1D lattice that realizes the photonic analog of the SSH model[9,12,13]. Here, the presence of qubit acts as a domain wall and thereby breaks the chiral symmetry of the chain. When the qubit energy lies in the bandgap of the waveguide, it induces a photonic bound states that is akin to an edge state and decays to either ends of the waveguide depending on the location of the qubit in the unit-cell. Note that these edge states are static photonic wavefunctions as opposed to moving currents seen in other edge states such as those in 2D topological insulators. Several proposals has also been reported to achieve in−situ tunable chiral photonic states which would then enable on-demand routing of quantum information in a network. To this end, a wQED platform based on a giant atom coupled to Josephson metamaterial has been proposed in ref. [14]. Here, the chiral bound state stems from the interference due to the non-local interaction induced by the giant atoms at different location in the waveguide. However, in order to flip the direction of the photon decay, one has to either tune the coupling between the qubit and the waveguide or dynamically alternate the impedance of the waveguide which is cumbersome in an experimental set-up.

In this work we propose a different chiral quantum system that utilizes just one frequency tunable qubit to switch the chirality of the (either photonic or electronic) bound state on-demand. In our model the waveguide is implemented by periodically modulating the on-site potentials and the hopping energy between the sites. Such a waveguide resembles the Rice-Mele model that can support both uni-directional and bi-directional edge states at different energies[15]. Furthermore we show that the directionality of these edges states can be switched by simply tuning the transition frequency of an artificial atom coupled to a defect site in the chain. In contrast to the previous proposal of ref. [14], our model offers the conditions where the states are perfectly directional with mathematically zero value of the wave-functions of the bound states on the 'wrong' side of the waveguide. We provide a detailed analysis by considering realistic experimental conditions such as finite nature of the device as well coupling to measurement leads. Moreover, we suggest two possible experimental realization of out wQED model that can be readily implemented using superconducting quantum circuits and quantum dot devices.

In addition to directional bounds states, there has been active research to develop chiral photonic interactions using giant atoms[16,17]. The tunable nature of these interactions arises by utilizing the non-local system topology, the nonlinear nature of the emitters as well as parametrically modulating the coupling between the two emitters. These proposals are used to generate directional emission and absorption of photons in the passband of the waveguide which can potentially used for transfer of quantum states, as well as the generation and manipulation of stabilizer codes for quantum error correction. Our proposal use static bound states in the stopband which has promise in realising long-range inter-qubit interactions while minimising crosstalk between adjacent qubits.

RESULTS

Directional edge states in Rice-Mele waveguide

Our goal is to create an in-situ tunable directional edge state that has all its population along one direction of the array while having

[1]ARC Centre of Excellence for Engineered Quantum Systems, School of Mathematics and Physics, The University of Queensland, Saint Lucia 4072 QLD, Australia. [2]Institute for Theory of Statistical Physics, RWTH Aachen University, Aachen 52056, Germany. ✉email: p.pakkiam@uq.edu.au

zero population along the other direction. Before we discuss how to tune the directionality, it is useful to review the chiral edge states supported by the Su-Schrieffer-Heeger (SSH) model[18]. As discussed in Supplementary Note 1, an SSH chain is an array of sites with alternating tunnel couplings t_1 and t_2 (with $t_2 > t_1$). This arrangement naturally introduces an energy spectrum that has two clusters of states with a large band gap in between. If every site has an adjacent site to which it is strongly tunnel coupled (that is, t_2), then no edge states occur and the band gap remains with no states. However, if there is a lonely site that is not tunnel coupled to another site with the stronger t_2, an edge state (rooting from the lonely site) with the desired directionality forms in the band gap. Many proposals to date have realised the edge states. However, the shortcomings are either in their sheer complexity (like giant atoms[14] or multiple qubits[8]) or the inability to switch the direction of the edge state in-situ[13].

Here, we propose a simpler approach that leads to the ability to switch the direction of the edge state by only varying the on-site potential of the tunable qubit site rooting the edge state. To create such a directional edge state, the intuitive approach is to merge two SSH chains to a central site. To point the edge-state along a given direction, we need to zero the population on the adjacent node on one side (to realise no edge-state in that direction like in Supplementary Fig. 1a) while letting the adjacent node on the other side have a non-zero population to spawn an edge-state (like in Supplementary Fig. 1b). However, the SSH model alone does not have enough degrees of freedom to tune the direction as there is no physical characteristic to differentiate both chains with respect to the central site. To circumvent this problem, we use a more general Rice-Mele model where the on-site potentials are alternated to break the inversion symmetry between both directions[15].

As shown in Supplementary Note 2, the tunable qubit needs to be side-coupled to a central site which joins the two Rice-Mele chains as shown in Fig. 1a. We couple the two Rice-Mele chains to the central site equally to have the resulting directional edge states symmetric when pointing leftward and rightward (see Supplementary Note 5 for more details). Additionally, this coupling is chosen to be the weaker t_1 to maximise the population away from the centre (qubit). As before, the on-site potentials must be different to break the inversion symmetry of the structure to enable directional edge states.

To get insight into operation of this device it is sufficient to consider just the four central sites highlighted in Fig. 1a via the Hamiltonian:

$$\mathbf{H}_{\text{y-cell}} = \begin{pmatrix} V_Q & -t_Q & 0 & 0 \\ -t_Q & V_C & -t_1 & -t_1 \\ 0 & -t_1 & -V & 0 \\ 0 & -t_1 & 0 & V \end{pmatrix}, \tag{1}$$

where the basis states (for the labelled sites) are $|Q\rangle$, $|C\rangle$, $|L\rangle$ and $|R\rangle$. This approximation holds (upon an appropriate renormalisation of the hopping t_1) when the qubit state exists within a large band gap opened by the two Rice-Mele chains as discussed in Supplementary Note 8. Figure 1b summarises the resulting energy spectrum observed when sweeping V_Q; the derivation of the features are given in Supplementary Note 4. We can switch between the leftward and rightward edge-states (sketched in the inset figures) $t_Q|L\rangle - t_1|Q\rangle$ and $t_Q|R\rangle - t_1|Q\rangle$ by rapidly sweeping V_Q past the anti-crossing at $V_Q = 0$. Note that the sweep rate must be faster than the anti-crossing gap: $\frac{2V}{\sqrt{2}} \cdot \frac{t_Q}{t_1}$ with the gap closing when $t_Q \to 0$ where the qubit is completely decoupled. The other corresponding states on the anti-crossing are bidirectional and lie near $E = 0$ as seen by their finite components in both $|L\rangle$ and $|R\rangle$ (again sketched in the inset). The two states near $E = \pm\sqrt{2}t_1$ are a part of the band states whereupon the remaining states of the Rice-Mele chains begin to appear as shown later in Fig. 1c.

Given the basic operation of the Y-structure, consider the full Hamiltonian of the Y-structure coupled to both Rice-Mele chains as described in Fig. 1a is:

$$\mathbf{H}_y = -t_Q|M\rangle\langle N| + \frac{V_Q}{2}|N\rangle\langle N|$$
$$- \frac{V}{2}|N_L\rangle\langle N_L| + \frac{V}{2}|N_R\rangle\langle N_R| - t_1\sum_{m=2p}^{N_R}|m\rangle\langle m+1| \tag{2}$$
$$+ \mathbf{H}_{\text{RM}}^{1,p} + \mathbf{H}_{\text{RM}}^{M+1,p} + h.c.$$

where the Hermitian conjugate applies to all listed terms. Here the length of the Rice-Mele chain is $2p$. That is, p is the number of pairs of sites coupled adjacently via t_2. The index of the central site is $M = 2N + 2$, with the adjacent site to the left being $N_L = M - 1$, the adjacent site on the right being $N_R = M + 1$, while the qubit site is on $N = 4p + 4$ (and incidentally the dimension of this Hamiltonian). Note that given p pairs, the dimension of the space spanned by $\mathbf{H}_{\text{RM}}^{m,p}$ is $2p$. The first two lines of the equation represent the central four sites interlinked via the tunnel couplings t_1 and modulating on-site potentials $\pm V$ (the factor of a half is due to the Hermitian conjugate). The qubit is tunnel-coupled via t_Q to the central site and has an on-site potential of V_Q. The Hamiltonians for the two interlinking Rice-Mele chains connecting to the central four sites are given via the tridiagonal matrix (when adding the Hermitian conjugate):

$$\mathbf{H}_{\text{RM}}^{n,p} = \frac{V}{2}\sum_{l=1}^{2p}(-1)^l|n+l-1\rangle\langle n+l-1|$$
$$- t_2\sum_{l=1}^{p}|n+2l-2\rangle\langle n+2l-1| \tag{3}$$
$$- t_1\sum_{l=1}^{p}|n+2l-1\rangle\langle n+2l|.$$

Here, the first line represents the modulating on-site potentials, while the last two lines represent the modulating tunnel couplings.

A numeric simulation of the Hamiltonian given in Eq. (2) is shown in Fig. 1c with 10-cell Rice-Mele chains. The eigenspectrum shows the band-gap along with the two expected gap states. When switching between $V_Q = \pm V$, the edge-state flips direction as seen by observing the corresponding eigenstates in Fig. 1d. Note that the edge-states are unidirectional with *exactly* zero probability on one side. The edge-state only has non-zero probability from the qubit-site onwards as expected from the 4-site model. This is in contrast to the tunable chiral quantum system proposed in ref. [14] where the chirality is not perfect and there is a finite probability of finding the photon on both the directions. Finally Fig. 1e shows how we can exploit the switchable edge states to have adjacent either qubits interact when the edge states face each other like the two on the left[13]. Similarly, adjacent qubits can have zero crosstalk when their edge states face away from one another like the two on the right.

Influence of measurement ports

The previous section introduced a Y-configuration that enables complete directional toggling of population along either side of the Rice-Mele chain. When running experiments to verify the presence of the edge states, the typical measurement will involve coupling the two edges of the chain to measurement ports. The influence of the ports on the resulting edge-states must be properly understood and thus, we apply the Green's function transport formalism[19,20]. First one has to write down the Hamiltonian for the Y-configuration with some finite Rice-Mele chains and then to add the non-hermitian self-energy terms Σ_n to the on-diagonal terms on sites n to account for the influence of the measurement ports. To see this explicitly, consider $\mathbf{H}_y$ with
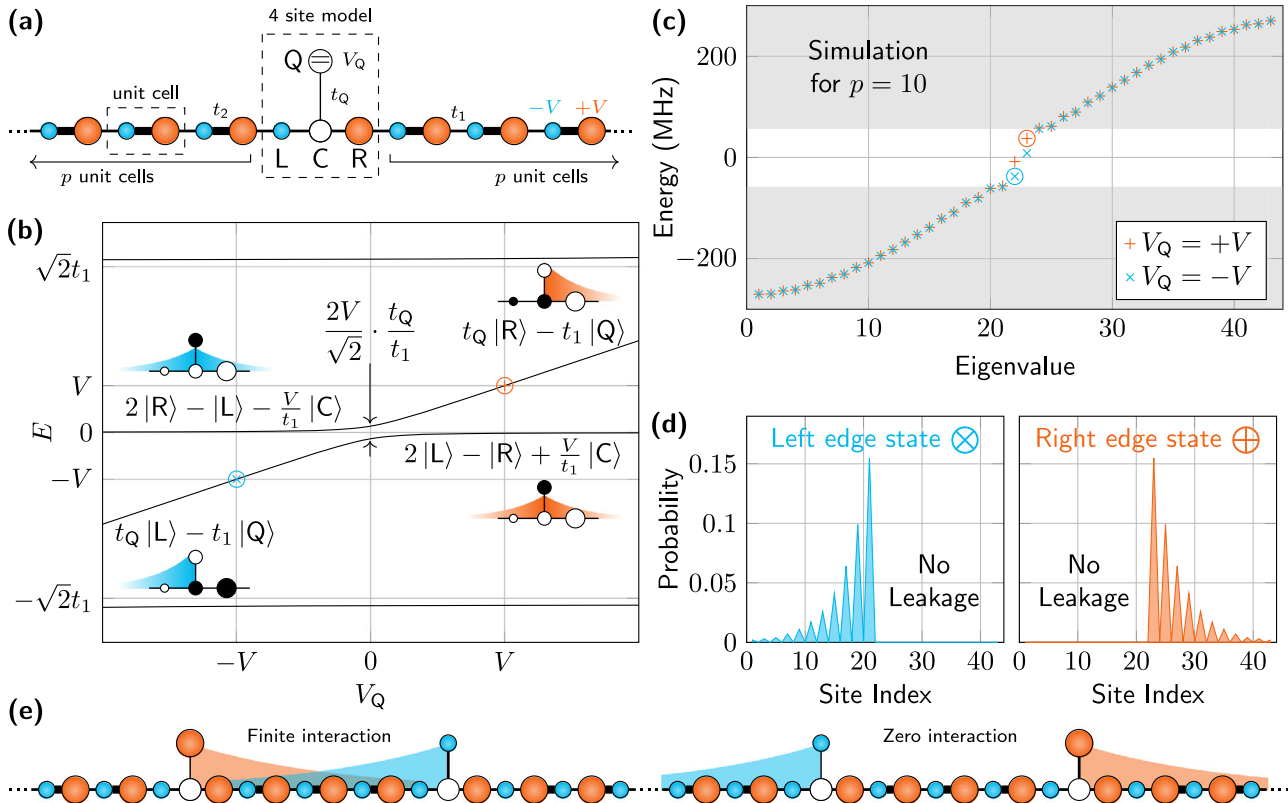
Fig. 1 Proposed Rice-Mele Y-coupler for qubits. The switching of the edge state is done by simply tuning the on-site potential of the qubit site. **a** Layout of the Rice-Mele coupler where a central site (in white) couples two Rice-Mele chains which have a modulating on-site potential (orange and blue for $+V$ and $-V$) and modulating tunnel coupling (t_1 and t_2 with $t_2 > t_1$). The qubit separately couples to the central site via tunnel coupling t_Q with itself having a tunable on-site potential V_Q. We term each strongly coupled pair of sites a 'unit cell' and the Rice-Mele chains each have p unit cells. The sites for the effective 4-site model in Eq. (1) are labelled Q, C, L and R. **b** Energy spectrum of the proposed Rice-Mele Y-model, shown in **a** with $V = V_R = -V_L$. The eigenstates producing the leftward and rightward edge-states are $t_Q|L\rangle - t_1|Q\rangle$ and $t_Q|R\rangle - t_1|Q\rangle$ and occur at $V_Q = -V$ and $V_Q = V$ respectively (shown by the blue and orange circles) as highlighted by sketched population on the two inset diagrams (with white for finite population while black for zero population). The remaining two eigenstates produce a bidirectional population spread as shown in the top-left and bottom-right inset diagrams. **c** Numeric simulation of the eigenvalues produced by the full coupler design described in Eq. (2). The simulation takes $V = 37.5$ MHz, $t_1 = 120$ MHz, $t_2 = 150$ MHz and $t_Q = 62.5$ MHz. There are $p = 10$ unit cells on both Rice-Mele chains. The spectra are plotted for both $V_Q = \pm V$. The non-shaded region indicates the band-gap which contains two gap states. The encircled edge states correspond to the operating points shown in **b**. **d** Occupation probabilities exposing the edge-states when taking the respective eigenvectors from the spectrum in **c**. Note that the occupation probability is zero on one side for both directional edge-states. The qubit site 44 has been omitted for clarity, while the site indices are enumerated from 1 to 43 from the most leftward site to the most rightward site (so 22 is the central site). **e** An example multi-qubit array where multiple edge states can be made to either overlap (finite interaction) or have zero crosstalk by simply switching the qubits' on-site potentials.

ports attached to the left most side 1 and the right most site N:

$$\mathbf{H}_y' = \mathbf{H}_y - i\Gamma(|1\rangle\langle 1| + |N\rangle\langle N|), \tag{4}$$

where we take the couplings Γ to be equal on both ports. The corresponding Green's function as a function of the energy $\hbar\omega$ is:

$$\mathbf{G}(\omega) = (\omega\mathbf{I}_N - \mathbf{H}')^{-1}, \tag{5}$$

where $\mathbf{I}_N$ is the identity matrix. Taking G_{ab} to be the matrix component (a, b) in $\mathbf{G}(\omega)$, we can write down the ports' transport transmission and reflection coefficients via the Fisher-Lee relations[19,21]:

$$S_{ab} = \delta_{ab} - 2i\Gamma G_{ab}, \tag{6}$$

where we opt to use the reverse sign convention for clarity. Noting that the physical S-parameters (that is, measured ratio of RF signals or DC currents entering or leaving the ports[19]) are given as $|S_{ab}|^2 \arg(S_{ab})$, we can numerically calculate the physical scattering parameters via the above relations. Nonetheless, by exploiting symmetries, we provide exact analytic solutions for this Hamiltonian in Supplementary Note 8. As the solutions are algebraically cumbersome, we shall focus on the

edge-states that occur at $\omega = V_Q$ when $V_Q = \pm V$. In this case, the transmission $S_{N1} = 0$. The reflectances when the edge-state faces port 1 are:

$$S_{11} = -1, V_Q = -V \tag{7}$$

$$S_{NN} = -\frac{1 + i\frac{2V}{\Gamma w_f}}{1 - i\frac{2V}{\Gamma w_f}}, V_Q = -V, \tag{8}$$

while the reflectances with the edge-state facing port N are:

$$S_{11} = -\frac{1 + i\frac{2V}{\Gamma w_f}}{1 - i\frac{2V}{\Gamma w_f}}, V_Q = V \tag{9}$$

$$S_{NN} = -1, V_Q = V \tag{10}$$

That is, the reflectance undergoes a relative π phase shift and reflects completely when probing an edge-state directed towards the measured port. Note that in the isolated regime where $\Gamma \to 0$, the reflectance of the opposite port is measured to remain at 1, which is the expected value given that there is no population near this port. However, we see that as $\Gamma \to \infty$, the opposite port also

yields the same phase in the reflected signal. That is, stronger coupling to the ports yields less chirality in the edge states as any macroscopic wavefunction will undergo greater losses to the ports. Note that w_f is the measure of edge state wavefunction's decay from the beginning to end of the Rice-Mele chain. In the limit where the states are away from the edges of the band-gap,
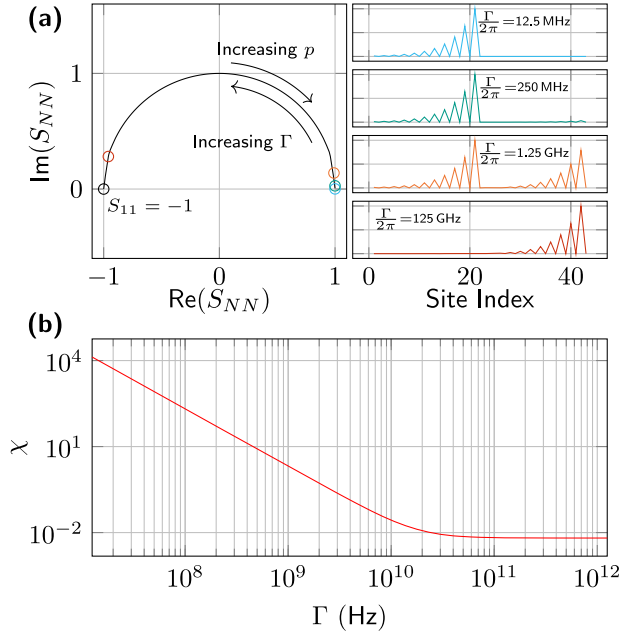

Fig. 2 Numeric simulation demonstrating the edge-states produced by the Y-structure when probing the reflectance on port 1 and N. The simulation takes $V = 37.5$ MHz, $t_1 = 120$ MHz, $t_2 = 150$ MHz and $t_Q = 62.5$ MHz. There are $p = 10$ cells of Rice-Mele chains. The leftward edge-state is initialised via $V_Q = -V$. **a** Here Γ is varied and the left panel shows the trajectory of S_{NN} on the Argand plane on increasing Γ. For four selected values of Γ, the resulting LDOS are plotted alongside (the qubit site is omitted in this plot for clarity). It is clear that the chirality of the wavefunction is slowly eroded with increasing Γ as population. In addition, the contrast used to distinguish the edge-state by comparing S_{11} and S_{NN} is also diminished. **b** Plot of associated chirality χ as the port coupling Γ is increased. The resulting edge-state spawning near port N causes a loss in chirality χ.

with the band-gap being large, we can approximate this term as:

$$w_f \approx \frac{t_2^2 - t_1^2}{t_2^2(t_2 t_1)^{2p} - t_1^2}. \tag{11}$$

Thus, for a small Rice-Mele chain where p is small, w_f tends to unity and the reflectance is limited by Γ. When p is large, w_f tends to zero as there is appreciable decay of the edge state leading to near zero population on the edge sites (1 or N). Thus, the Γ term is overcome, yielding a lower port coupling, to give a reflection of 1.

Figure 2a shows the changing S_{NN} when probing an edge-state facing port 1. It is once again clear that when Γ is increased, the reflectance moves about the semi-circle from $S_{NN} = 1$ to $S_{NN} = -1$. In doing so, the local density of states (LDOS) shifts (details of its calculation are given in Supplementary Note 10) from a strongly chiral edge-state with all population exclusively on the left hand side to being on sides. The interpretation is that when a strongly coupled port makes site N starts to dominate the adjacent tunnel coupling $\Gamma \gg t_2$ (thereby, making a large energy cost to occupy site N), the site $N - 1$ starts to become isolated from site N. Thus, like in Fig. 1 in Supplementary Note 1, an edge-state forms from site N. A similar edge state does not form from site 2 as it is effectively zeroed on this site by the main edge-state from the central site. We can now define a simple chirality factor:

$$X = \frac{\sum_{n=1}^{M-1} P_n}{\sum_{n=M+1}^{N} P_n}, \tag{12}$$

where P_n is the occupation probability at site n given the LDOS. By definition, $\chi = \infty$ when there are no ports. When increasing Γ to move from $S_{NN} = 1$ to $S_{NN} = -1$, the resulting change in chirality is shown in Fig. 2b. The chirality drops quadratically until it settles at a steady-state value whereupon the central edge-state and the edge-state at port N settle to the limit where the port coupling fully isolates site $N - 1$.

Implementation

The proposed structure for a switchable edge state can be implemented either as photonic edge-states in circuit quantum electrodynamics (cQED) or electronic edge-states in conventional quantum dot system. This section highlights the details in design and implementation for both platforms.

The Y-structure and the associated Rice-Mele chains can be implemented using cQED elements. An example implementation of a $p = 4$ Y-structure in Fig. 3a is shown in Fig. 3b. We implement
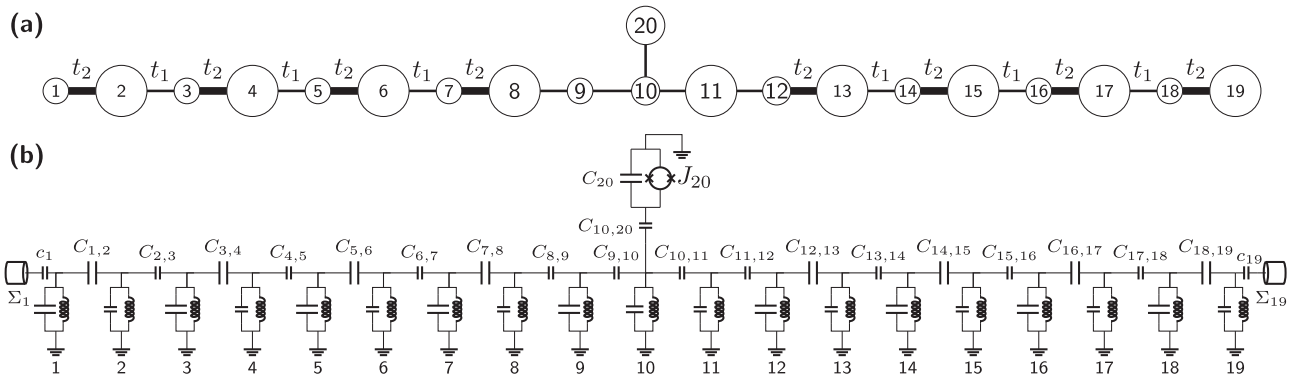

Fig. 3 Implementing the Rice-Mele Y-coupler using cQED elements. The individual sites are formed with resonators while the tunnel couplings are implemented with coupling capacitors. **a** A simple coupled using chains with $p = 4$ cells. Site 20 has a tunable on-site energy. **b** Implementing the structure shown in **a** using cQED elements. Each site m has a resonator comprising of a capacitor C_m and inductor L_m (not labelled for clarity). The resonant frequencies alternate with the on-site potentials (shown via the larger and smaller capacitances for smaller and larger on-site potentials respectively). The tunnel couplings are implemented via capacitors $C_{m,n}$. The capacitances $C_{m,n}$ are also shown to alternate to account for the modulating t_1 and t_2 (being smaller and larger capacitances respectively). The tunable element is implemented via a flux-tunable Transmon qubit. If this structure is not coupled to other qubits and is just being measured via two ports, the circuit will contain two transmission lines Σ_1 and Σ_{19} with coupling capacitors c_1 and c_{19}.
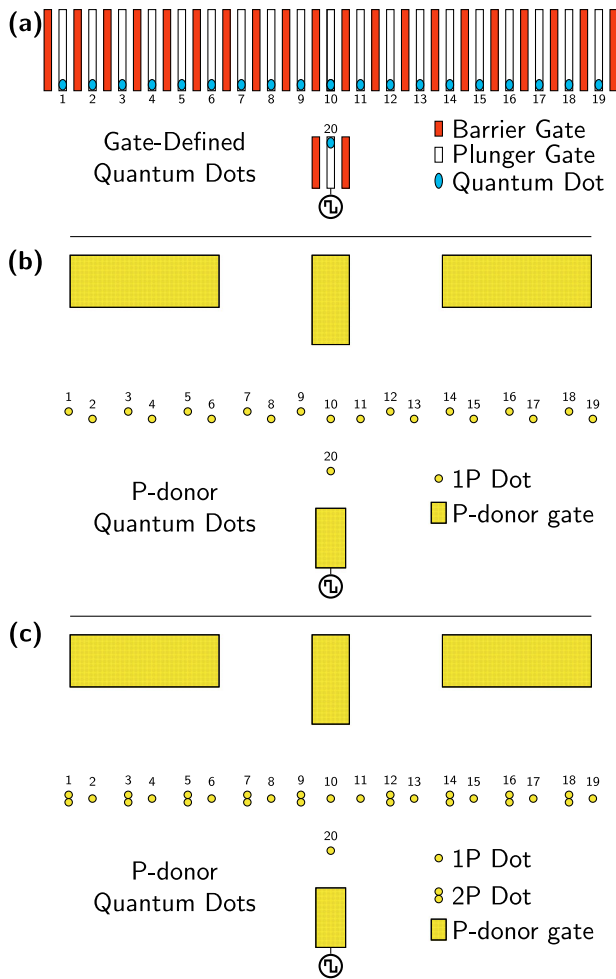
Fig. 4 Implementing the Rice-Mele Y-coupler using quantum dots. In each case, the outlined gates have constant voltage biases that are tuned once on startup. To rapidly control the direction of the bound state on demand, we highlight the single gate that requires DC pulsing. **a** Implementation using gate-defined quantum dots. The $p = 4$ structure is given in Fig. 3a. The confinement potential formed by the gates traps the electrons into small quantum dots. The barrier gates can be used to in-situ tune the confinement potentials, while the plunger gates enable in-situ tuning of the on-site potentials. Thus, one may tune the parameters to form the required Rice-Mele chains. **b** When using STM patterned Si-P quantum dots, there is no need for dedicated confinement gates. The tunnel couplings are set by varying the distances between the P-donor dots (dots closer together had larger tunnel couplings), while the on-site potentials are tuned in-situ via the P-donor gates on the top (dots closer to the gates are tuned more strongly). Only the gate closest to site 20 is reservoir-coupled to the dot and is used to load electrons into the array. **c** The STM-patterned structure can be modified to provide alternating on-site potentials via larger 2P-donor dots. In this case, the on-site potentials dominate the tunnel couplings, whereupon we utilise the large T_1 and T_2^* times of electron spins in P-donor dots. This regime of operation is discussed in Supplementary Note 3.

each site n with an LC-oscillator (consisting of C_n and L_n) where its resonant frequency corresponds to the on-site potential. The tunnel-couplings are achieved via capacitors connecting across the resonators ($C_{n,n'}$ across resonators or sites n and n'). The tunable side-coupled site (in this example, site 20) is achieved via a flux tunable Transmon qubit. The resulting edge states are photonic edge states across multiple resonators. As discussed in Supplementary Note 6, the corresponding on-site potentials

$V_n \in \{V, -V\}$ and tunnel-couplings $t_{n,n'} \in \{t_1, t_2, t_Q\}$ are:

$$V_n = \frac{\hbar}{\sqrt{L_n C_{n(B)}}} - \hbar\omega_0 \tag{13}$$

$$t_{n,n'} = -\frac{\hbar\sqrt{Z_n Z_{n'}}}{2 C_{n(B)} C_{n'(B)}} C_{n,n'}, \tag{14}$$

where $C_{n(B)}$ is the sum total of all capacitances connected to site n and $Z_n = \sqrt{C_{n(B)}/L_n}$ with the important assumption: $C_{n,n'} \ll C_{n(B)}$. Since the Rice-Mele chain requires a modulation of positive and negative energies, we globally offset the on-site energies by $\hbar\omega_0$. Note that $\hbar\omega_0$ vertically recenters the spectrum in Fig. 1b. Choosing a global nominal inductance $L_n = L_0$, we can solve for $C_{n(B)}$. Thus, we obtain the $C_{n,n'}$ for a given $t_{n,n'}$. Note that $C_{n,n'}$ is linearly proportional to $t_{n,n'}$ as shown in Fig. 3. On obtaining all the $C_{n,n'}$ terms, we can finally obtain the resonator capacitances C_n.

Given that the cQED implementation will likely be tested via probing ports on the end sites (sites 1 and 19 in the example given in Fig. 3), it is useful to understand the parameters concerning the coupling of the array to these ports. As discussed in Supplementary Note 6, the port couplings can be modelled via the self-energy term given by:

$$\Sigma_n = \Delta\omega_n - i\frac{\kappa_n}{2}, \tag{15}$$

where the frequency shift and photon loss rate are given as:

$$\Delta\omega_n \approx \frac{\omega_n}{\sqrt{1 + \frac{c_n}{C_n}}} - \omega_n \tag{16}$$

$$\kappa_n \approx \frac{c_n^2 R}{C_n^2 L_n}, \tag{17}$$

Note that the idea is that the lead connecting to site n has a resistance R (typically 50 Ω) and a coupling capacitor c_n satisfying the limit $c_n \ll C_n$. Additionally, note that $\Gamma_n = \kappa_n/2$. Supplementary Note 7 shows the SPICE simulations done on the model shown in Fig. 3 to verify the expressions for the individual lumped elements.

Due to the fixed values in the inductors and capacitors, it is important to consider the effect of fabrication defects on the final chiralities. As discussed in Supplementary Note 7, numerical simulations using a modest fabrication precision yielding 1% variation in V, t_1 and t_2, yields a spread of $\chi = 1130 \pm 80$ for a typical port-coupled implementation. In the case of no port-couplings (that is, coupling the chains to adjacent qubits like in Fig. 1e), the median chirality drops from infinity to be bounded by the 5th and 95th quantiles as: 48000 (6×10^3, 6×10^6). The sustained chirality confirms the fact that the states in the band-gap of a Rice-Mele or SSH waveguide are protected from localised defects as the wavefunction is macroscopically spread over multiple sites to effectively average out the effect of defects.

Given that the structure given in Eq. (2) describes a network of tunnel-coupled sites with individual on-site potentials, a natural implementation falls directly in quantum dots. The chiral bound states are now electronic wavefunctions as opposed to the photonic wavefunctions seen when implementing in cQED. The required array is compatible with all major quantum dot platforms.

In the case of gate-defined quantum dots in Fig. 4a (such as SiGe or CMOS), the tunable tunnel couplings and on-site potentials enable a fully configurable array that can account for local defects[22,23]. Note that the outlined gates require constant DC biases, provided by DC looms, that can be rapidly tuned once on startup[23–27]. Afterwards, the direction of the bound state is rapidly controlled via DC pulses, sent through wide-band coaxial lines, on the central gate controlling to the qubit.

Another approach is to use atomic precision STM (scanning tunnelling microscope) patterned Si-P quantum dots where single

P-donors are placed within a silicon substrate[28–30]. The P-donor dots yield a trapping potential without the need for confinement gates. To alternate the tunnel-couplings the distances between the dots are alternated with shorter distances used for the higher tunnel coupling t_2. As shown in Fig. 4b, the on-site potentials can be alternated by staggering the alternate dots closer to tuning gates. As dots are typically spaced in the order of 12 nm to create tunnel-couplings in the order of 10 GHz, the on-site potentials only need to be tuned to approximately 1 GHz or approximately 4 μeV. Thus, the gates need to be only tuned approximately 100 μV for typical lever-arm α values.

An alternative approach using P-donor quantum dots utilises the ability to tune the depth of the on-site potentials by placing another P-donor in the dot (a 2P cluster) like in Fig. 4c. In this case, depending on the positions of the P-donors in the Si crystal, the on-site potentials can vary in the order of 1 meV or 200 GHz[31]. In such a case, the tunnel-couplings can be feasibly set in the order of 50 GHz[32]. Thus, the on-site potentials dominate the tunnel couplings as in the case discussed in Supplementary Note 3. In such a case, the edge-state can be tuned to be leftward, rightward or completely localised to the central qubit dot. Although this configuration was discouraged earlier, in the case of Si-P dots, the large electron spin T_1 and T_2^* times may make this a desirable configuration[33]. That is, the electron spin can be localised and made to interact with neighbouring qubits on demand with zero crosstalk to other adjacent qubits.

It should be noted that the outlined proposals for the quantum dot structures require extra tuning gates (albeit, minimal with the Si-P implementations) compared to typical multi-qubit architectures. However, these are simply DC tuning gates that are only required to be tuned once to achieve the long-distance coupling with zero crosstalk between adjacent qubits. Whereas, a proposal that uses a normal quantum dot array through which to shuttle electrons (to mitigate crosstalk via distance) will require multiple fast-pulse gates[34]. One notes that fast-pulse gates are more spatially expensive for they are extra coaxial lines in the dilution fridge as opposed to a compact DC wire loom.

DISCUSSION

We have shown a general structure that can realise directional edge states with perfect chirality and in-situ switching via Rice-Mele chains. The direction can be switched by simply tuning the on-site potential of a single site; a feat that is easily realised in both cQED (via flux tuning) and quantum dot implementations (via gate voltage tuning). We show how our model can be implemented in cQED via a universal translation recipe that can be used to implement arbitrary site models using cQED elements. In addition, we show that the Rice-Mele chains can be implemented in quantum dot arrays in both the gate-defined and atomically defined quantum dot platforms. Finally, we provide a complete analysis of the influence of measurement probes. That is, although our model has zero crosstalk when coupling adjacent qubits, we show that there is a marginal loss in chirality when coupling the array to measurement probes in the case of verifying the directionality of a single qubit edge state. The overall simplicity of design and implementation shows promise in realising long-range inter-qubit interactions while minimising crosstalk between adjacent qubits.

DATA AVAILABILITY

The datasets generated during and/or analysed during the current study are available from the corresponding author on reasonable request.

REFERENCES

1. Kimble, H. J. The quantum internet. *Nature* **453**, 1023–1030 (2008).
2. Cirac, J. I., Ekert, A. K., Huelga, S. F. & Macchiavello, C. Distributed quantum computation over noisy channels. *Phys. Rev. A* **59**, 4249–4254 (1999).
3. Lodahl, P. et al. Chiral quantum optics. *Nature* **541**, 473–480 (2017).
4. Hamann, A. R. et al. Nonreciprocity realized with quantum nonlinearity. *Phys. Rev. Lett.* **121**, 123601 (2018).
5. Sun, S., Kim, H., Luo, Z., Solomon, G. S. & Waks, E. A single-photon switch and transistor enabled by a solid-state quantum memory. *Science* **361**, 57–60 (2018).
6. Wanjura, C. C., Brunelli, M. & Nunnenkamp, A. Topological framework for directional amplification in driven-dissipative cavity arrays. *Nat. Commun.* **11**, 3149 (2020).
7. Ramos, T., Vermersch, B., Hauke, P., Pichler, H. & Zoller, P. Non-markovian dynamics in chiral quantum networks with spins and photons. *Phys. Rev. A* **93**, 062104 (2016).
8. Pichler, H., Ramos, T., Daley, A. J. & Zoller, P. Quantum optics of chiral spin networks. *Phys. Rev. A* **91**, 042116 (2015).
9. Bello, M., Platero, G., Cirac, J. I. & González-Tudela, A. Unconventional quantum optics in topological waveguide QED. *Sci. Adv.* **5**, eaaw0297 (2019).
10. Söllner, I. et al. Deterministic photon–emitter coupling in chiral photonic circuits. *Nat. Nanotechnol.* **10**, 775–778 (2015).
11. Mitsch, R., Sayrin, C., Albrecht, B., Schneeweiss, P. & Rauschenbeutel, A. Quantum state-controlled directional spontaneous emission of photons into a nanophotonic waveguide. *Nat. Commun.* **5**, 5713 (2014).
12. Su, W. P., Schrieffer, J. R. & Heeger, A. J. Solitons in polyacetylene. *Phys. Rev. Lett.* **42**, 1698–1701 (1979).
13. Kim, E. et al. Quantum electrodynamics in a topological waveguide. *Phys. Rev. X* **11**, 011015 (2021).
14. Wang, X., Liu, T., Kockum, A. F., Li, H.-R. & Nori, F. Tunable chiral bound states with giant atoms. *Phys. Rev. Lett.* **126**, 043602 (2021).
15. Rice, M. J. & Mele, E. J. Elementary excitations of a linearly conjugated diatomic polymer. *Phys. Rev. Lett.* **49**, 1455–1459 (1982).
16. Guimond, P.-O. et al. A unidirectional on-chip photonic interface for superconducting circuits. *npj Quant. Inform.* **6**, https://doi.org/10.1038/s41534-020-0261-9 (2020).
17. Joshi, C., Yang, F. & Mirhosseini, M. Resonance fluorescence of a chiral artificial atom https://arxiv.org/abs/2212.11400 (2022).
18. Su, W. P., Schrieffer, J. R. & Heeger, A. J. Solitons in polyacetylene. *Phys. Rev. Lett.* **42**, 1698–1701 (1979).
19. Datta, S. *Electronic Transport in Mesoscopic Systems* (Cambridge University Press, 1997).
20. Maurer, M. T. et al. Quantum dot coupled to topological insulators: the role of edge states. *Phys. Rev. B* **105**, 115419 (2022).
21. Fisher, D. S. & Lee, P. A. Relation between conductivity and transmission matrix. *Phys. Rev. B* **23**, 6851–6854 (1981).
22. Hensgens, T. et al. Quantum simulation of a fermi–hubbard model using a semiconductor quantum dot array. *Nature* **548**, 70–73 (2017).
23. Mills, A. R. et al. Shuttling a single charge across a one-dimensional array of silicon quantum dots. *Nat. Commun.* **10**, 1063 (2019).
24. Moon, H. et al. Machine learning enables completely automatic tuning of a quantum device faster than human experts. *Nat. Commun.* **11**, 4161 (2020).
25. Zwolak, J. P. et al. Autotuning of double-dot devices in-situ with machine learning. *Phys. Rev. Appl.* **13**, 034075 (2020).
26. Ziegler, J. et al. Toward robust autotuning of noisy quantum dot devices. *Phys. Rev. Appl.* **17**, 024069 (2022).
27. Zwolak, J. P. & Taylor, J. M. Colloquium: advances in automation of quantum dot devices control. *Rev. Mod. Phys.* **95**, 011006 (2023).
28. Fuechsle, M. et al. A single-atom transistor. *Nat. Nanotechnol.* **7**, 242–246 (2012).
29. Hill, C. D. et al. A surface code quantum computer in silicon. *Sci. Adv.* **1**, e1500707 (2015).
30. Kiczynski, M. et al. Engineering topological states in atom-based semiconductor quantum dots. *Nature* **606**, 694–699 (2022).
31. Weber, B. et al. Spin blockade and exchange in coulomb-confined silicon double quantum dots. *Nat. Nanotechnol.* **9**, 430–435 (2014).
32. Pakkiam, P., House, M. G., Koch, M. & Simmons, M. Y. Characterization of a scalable donor-based singlet–triplet qubit architecture in silicon. *Nano Lett.* **18**, 4081–4085 (2018).
33. Pla, J. J. et al. High-fidelity readout and control of a nuclear spin qubit in silicon. *Nature* **496**, 334–338 (2013).
34. Fujita, T., Baart, T. A., Reichl, C., Wegscheider, W. & Vandersypen, L. M. K. Coherent shuttle of electron-spin states. *npj Quant. Inform.* **3**, 22 (2017).

AUTHOR CONTRIBUTIONS
The four-site model was developed by P.P. and M.P. The numeric simulations were handled by P.P. and N.P.K. Development of the Green's function formalism to handle the influence of ports was done by M.P. The formalism to implement in cQED was developed by P.P., N.P.K. and A.F. The project was supervised by A.F.

COMPETING INTERESTS
The authors declare no competing interests.

ADDITIONAL INFORMATION
Supplementary information The online version contains supplementary material available at https://doi.org/10.1038/s41534-023-00722-8.

Correspondence and requests for materials should be addressed to Prasanna Pakkiam.

Reprints and permission information is available at http://www.nature.com/reprints

Publisher's note Springer Nature remains neutral with regard to jurisdictional claims in published maps and institutional affiliations.